

Enhancing affinity of neutralizing SARS-CoV-2 nanobody through facile structure-guided mutations in CDRs

Vishakha Singh, Mandar Bhutkar, Shweta Choudhary, Sanketkumar Nehul, Rajesh Kumar, Jitin Singla, Pravindra Kumar, Shailly Tomar*.

Department of Biosciences and Bioengineering, Indian Institute of Technology Roorkee, Uttarakhand, India.

*Corresponding author address: Department of Biosciences and Bioengineering, Indian Institute of Technology Roorkee, Roorkee-247667, Uttarakhand, India; Email id: shailly.tomar@bt.iitr.ac.in

Shailly Tomar

Professor,
Department of Biosciences and Bioengineering,
Indian Institute of Technology Roorkee,
Uttarakhand, India 247667
Tel: +91-1332-285849
Fax: 91-1332-273560
Email: shailly.tomar@bt.iitr.ac.in
ORCID ID: 0000-0002-1730-003X

Abstract:

The optimization of antibodies to attain the desired levels of affinity and specificity holds great promise for development of the next generation therapeutics. This study delves into the refinement and engineering of CDRs through *in silico* affinity maturation followed by binding validation using ITC and pseudovirus-based neutralization assays. Specifically, it focuses on engineering CDRs targeting the epitopes of RBD of the spike protein of SARS-CoV-2. A structure-guided virtual library of 112 single mutations in CDRs was generated and screened against RBD to select the potential affinity-enhancing mutations. Subsequent biophysical

studies using ITC provided insights into binding affinity and key thermodynamic parameters. Consistent with *in silico* findings, seven single mutations resulted in enhanced affinity. The mutants were further tested for neutralization activity against SARS-CoV-2 pseudovirus. L106T, L106Q, S107R, and S107Q generated mutants were more effective in virus-neutralizing with IC₅₀ values of ~0.03 μM, ~0.13 μM, ~0.14 μM, and ~0.14 μM, respectively as compared to the native nanobody (IC₅₀ ~0.77 μM). Thus, in this study, the developed computational pipeline guided by structure-aided interface profiles and thermodynamic analysis holds promise for the streamlined development of antibody-based therapeutic interventions against emerging variants of SARS-CoV-2 and other infectious pathogens.

Keywords: CDRs mutations, *In silico*, Affinity maturation, SARS-CoV-2, Pseudovirus,

Introduction:

The development of advanced biologic therapeutics, including monoclonal antibodies (mAbs), single-domain antibodies (sdAb) or nanobodies (Nb), and engineered proteins, revolves around enhancing their ability to effectively bind to the specific molecular targets associated with diseases, commonly referred to as antigens. The term “Bio-better” is defined for the biotherapeutic molecules, such as antibodies or proteins, that have been improved to exhibit superior characteristics compared to their original or conventional counterparts¹. These improvements could be in terms of efficacy, safety, tolerability, or other desirable properties, presenting a promising strategy for the development of next generation therapeutics^{1,2}. The impeccable specificity and high affinity of antibodies are increasingly exploited for therapeutic and diagnostics purposes³⁻⁵. In the process of discovery and development of antibodies, immunization of animals and various display methods (phage, yeast, and ribosome) serve as fundamental techniques^{6,7}. However, reaching the desired levels of affinity and specificity

against targeted antigens using traditional approaches may not be consistently successful. Thereby, affinity maturation becomes a valuable strategy to further optimize the binding affinity of antibodies. In nature, this process occurs naturally in the B-cells, in which the host immune system generates high-affinity antibodies against specific antigens through somatic hypermutation^{8,9}. Several *in vitro* techniques based on directed evolution aim to mimic this natural process. However, this daunting task of enhancing the affinity using *in vitro* methods is rather complicated, expensive, and time-consuming. Structure-based computational engineering offers an attractive alternative strategy for the development of biotherapeutic antibodies^{10–12}.

Affinity maturation can be expedited and simplified through computational methods, specifically by employing random virtual mutagenesis guided by the structure-aided interface profiles of antibodies and antigens. This multifaceted task includes structure determination/prediction, identification of binding interface, and calculation of mutational energy changes. The availability of high-quality structural data of antigen and antibody complexes serves as a crucial reference point for the *in silico* affinity maturation process¹³. The antigen-binding specificity of antibodies is primarily dictated by paratopes, the specialized regions on the molecule responsible for interaction with antigens. Within these paratopes, CDRs (Complementarity-determining regions) play a pivotal role in diversifying and optimizing antibody affinity. Conversely, the remaining framework regions (FRs) contribute significantly to the overall structural integrity of the antibody molecule^{14–16}. To attain a high binding affinity against antigens, antibodies require surface complementarity in terms of shape, size, and chemical nature to ensure effective recognition and interaction with the target antigens. Shape complementarity relies on the aromatic residues that bring the two surfaces together primarily through Van der Waals and hydrophobic interactions. Specificity and strength, on the other hand, are contributed by the electrostatic interactions i.e., salt bridges

formed between charged side chains, along with hydrogen bonds connecting oxygen and/or nitrogen atoms^{17,18}. *In silico* affinity maturation has been successfully applied to develop high-affinity antibody fragments such as fragment antigen-binding region (Fabs), Single-chain variable fragments (scFvs), and Variable Heavy domain of Heavy chain (VHHs) against numerous antigens^{19–24}.

VHHs are the antigen binding domain of only heavy chain antibodies that are derived from the camelid's animals and are also referred to as nanobodies²⁵. Nanobodies, with their compact dimensions of approximately 15 kDa, offer distinct advantages such as specificity, thermodynamic stability, enhanced target engagement, and deeper tissue penetration compared to traditional antibodies. Notably, their smaller molecular size and increased stability simplify the processes of cloning, expression, and purification, allowing for high yields in bacterial, yeast, and mammalian expression systems^{26–32}. The COVID-19 pandemic has accelerated extensive efforts in the field of development and engineering of neutralizing nanobodies against severe acute respiratory syndrome coronavirus 2 (SARS-CoV-2). Despite extensive vaccine administration drives, concerns persist regarding increased transmissibility, immunological resistance, and waning immunity, potentially leading to more severe infection waves³³. A critical initial step of infection involves cell entry of viral particles facilitated by the interaction between the spike protein (S-protein) of SARS-CoV-2 and the angiotensin-converting enzyme 2 (ACE2) receptor on the host cell. The receptor-binding domain (RBD) of S-protein, comprises critical residues binding to ACE2, and emerges as a key player in virus entry, offering an attractive target for suppressing and inhibiting virus infection³⁴. Of the other structural proteins of SARS-CoV-2, the S-protein has been recognized as a prime target for the development of neutralizing antibodies^{35–37}. Numerous studies on therapeutics against SARS-CoV-2 have accentuated the efficacy of nanobodies targeting the RBD of the S-protein^{38–48}. These nanobodies neutralize the virus by either directly competing with ACE2 for the same

epitope (Ty1, H11-H4, C5, and H3) or by interacting with the non-RBD region of the SARS-CoV-2 S-protein (F2, C1, and VHH72)^{41–44,49}. The incessant emergence of highly contagious escape variants has reinforced the global threat of SARS-CoV-2, necessitating efficient preventive or therapeutic strategies to mitigate any future risks^{50,51}. Global surveillance efforts utilizing genome sequencing unveiled over 5000 amino acid alterations within the genome of SARS-CoV-2, including substitutions, deletions, and insertions, predominantly concentrated within the S-protein⁵². This demands the need for quick strategies to upgrade the available vaccines and therapeutics for continued efficacy against emerging variants.

Utilizing insights obtained from the crystal structure of the SARS-CoV-2 RBD in complex with nanobody (H11-H4) (PDB: 6ZBP), computational predictions, and *in vitro* validation were employed to engineer and generate high-affinity mutants of the H11-H4 nanobody (referred to native nanobody in this paper). A comprehensive *in silico*, biophysical characterization, and efficacy testing investigations were conducted on a set of 9 mutants that were screened from an *in house* library of 112 single mutants of native nanobody. Using, Isothermal Titration Calorimetry (ITC), the binding affinities of both native and mutant nanobodies were assessed against RBD, aiming to identify the high affinity binders. Pseudovirus neutralization assay successfully identified four mutants of nanobody with significantly improved neutralizing activity compared to their native counterparts. This integrated approach shows potential in expediting the development of antibody based therapeutic interventions targeting emerging variants of SARS-CoV-2 and other pathogens.

Material and methods:

Software and hardware used for *in silico* study:

Protein structures were retrieved from the RCSB-PDB⁵³, and their IDs are indicated as they appear in the text. For structural visualization, PyMol and Crystallographic Object-Oriented

Toolkit (Coot)⁵⁴ were utilized, and Coot was also used for introducing the mutations in the nanobody. Structural comparison and interaction studies were accomplished using PyMol⁵⁵ and LigPlot+⁵⁶. Docking was performed by protein-protein docking software, HADDOCK 2.4⁵⁷. Molecular simulation studies were carried out using Gromacs 2022.2 suite⁵⁸ on an Ubuntu-based LINUX workstation.

Comprehensive *in silico* mutagenesis:

For the computational studies, the coordinates of SARS-CoV-2 RBD and native nanobody (H11-H4) were extracted from the PDB ID: 6ZBP⁴³. A docked complex of the native nanobody and the RBD was generated using HADDOCK 2.4⁵⁹. The complex was used as the reference for all the computational studies and for mapping the interacting residue present between the RBD and native nanobody using PyMol and LigPlot+ software. The coordinates of the native nanobody were further used for *in silico* affinity maturation. The first step of *in silico* affinity maturation involves virtual mutagenesis where single mutations were introduced in the selected residues of the CDRs of the nanobody using Coot software, generating a library of nanobody mutants^{60,61}. In Coot, mutations are introduced individually, allowing us to predict their stereochemical effects. The initial position for the new rotamer is chosen based on the most probable orientation⁵⁴. The substitution mutation was performed majorly to charged, polar, and aromatic residues. Also, mutations to proline, glycine, and cysteine were avoided owing to the peculiar nature of these amino acids. Subsequently, the 3D structures of these mutants were energy-minimized using the CHARMM 27 force field⁶² in the Gromacs 2022.2 suite. The generated library of nanobody mutants was screened against RBD (Coordinate extracted from 6ZBP) using HADDOCK 2.4 with default parameters. These docked complexes were further screened, employing criteria such as docking scores and favourable interactions compared to the native nanobody complex.

and *XhoI* restriction sites with an N-terminal histidine tag. Subsequently, the recombinant vector was transformed into competent *E. coli* DH5 α cells and grown on Luria Bertani (LB) agar plates supplemented with 50 μ g/mL kanamycin overnight at 37 °C. The following day, kanamycin-positive colonies were selected from the agar plate and plasmids were extracted using the MiniPrep isolation kit (Qiagen, USA). The cloned construct was eventually confirmed using Sanger sequencing.

Site-directed mutagenesis (SDM):

After confirming the plasmid through Sanger sequencing, site-directed mutagenesis was performed to introduce selected mutations in the CDRs of the native nanobody. Specifically designed overlapping primers were used for the PCR amplification of the native nanobody gene. The amplification process individually introduced 9 single mutations, resulting in one amino acid change per mutation. Following the amplification, the parental strand was enzymatically cleaved using *DpnI*, and digested product was transformed into competent XL-1 blue cells of *E. coli* and grown on the LB agar plates containing kanamycin (50 μ g/mL) and chloramphenicol (35 μ g/mL). The following day, positive colonies were picked from the agar plate and the plasmids were isolated. These plasmids were sent for Sanger sequencing to confirm the presence of the intended mutations in the nanobody gene. The list of primers employed for site-directed mutagenesis are listed in (Supplementary Table 2).

Recombinant nanobody production:

The recombinant plasmid with the cloned nanobody gene was transformed into competent *E. coli* Rosetta cells (DE3; Novagen, USA) and grown on LB agar plates containing kanamycin (50 μ g/mL) and chloramphenicol (35 μ g/mL). For bacterial expression of nanobody protein, a single colony was picked and inoculated into 10 mL of LB broth supplemented with kanamycin (50 μ g/mL) and chloramphenicol (35 μ g/mL), and the culture was incubated at 37 °C and

200 rpm overnight. This primary culture was used to inoculate the 1 L LB broth, culture was grown at 37 °C till optical density (OD) OD₆₀₀ reached 0.4. Subsequently, recombinant nanobody protein was expressed by adding 0.2 mM isopropyl-β-d-1-thiogalactopyranoside (IPTG) as inducer, and culture was grown at 16 °C for 20 h in an incubator shaker at 180 rpm. Following this, the cells were harvested by centrifugation at 4 °C at 6,000 rpm for 10 min. The cell pellet was then resuspended in the lysis buffer (50 mM Sodium Phosphate, 500 mM NaCl, and 10 mM Imidazole, pH 8.0). Cell disruption was done using a French press (Constant Systems Ltd, Daventry, England) and the cellular debris was removed by centrifugation of cell lysate at 10,000 rpm for 90 min at 4 °C. The clarified supernatant was loaded onto a pre-equilibrated gravity flow column of nickel-nitrilotriacetic acid (Ni-NTA) beads (Qiagen, Germantown, MD, USA). The column was washed with the increasing concentration of imidazole and the recombinant nanobody protein was eluted at a gradient of 250-500 mM imidazole concentration in elution buffer (50 mM Sodium Phosphate, 300 mM NaCl, and 5% glycerol, pH 8.0). Fractions collected at different imidazole concentrations were analyzed using 15% sodium dodecyl sulphate-polyacrylamide gel electrophoresis (SDS-PAGE) to confirm the purity of purified nanobody proteins (Supplementary Fig 1A). Fractions containing the pure nanobody protein were pooled together, dialyzed against 1 X phosphate-buffered saline (PBS) containing 140 mM NaCl, 2.6 mM KCl, 10 mM NaHPO₄·2H₂O and 1.8 mM KH₂PO₄ pH 7.4 with 10% glycerol for overnight at 4 °C. After dialysis the protein was concentrated through Amicon centrifugal filters (Millipore, Burlington, MA, USA) with a molecular weight cutoff of 3 kDa. The concentrated protein was flash frozen in liquid nitrogen and stored at -80 °C until further use. The expression and purification of all nanobody mutants were carried out similarly.

Recombinant RBD production:

The expression and purification for SARS-CoV-2 RBD (residues 319-528) was conducted following the previously reported protocol with some modifications⁶³. In brief, the RBD gene

was cloned in pPick.9 vector in between the *AvrII* and *SnaBI* restriction sites. Upon confirming the clone through Sanger sequencing, the plasmid was linearised with *Sall* enzyme and used for transfection into competent *Pichia pastoris* cells via electroporation. The transfected cells were grown on a histidine-deficient medium for 2-3 days. Positive colonies were screened using a gentamycin gradient to identify colonies with high expression of the RBD protein. Selected colonies were subjected to a small-scale expression of RBD, and the maximum protein yielding colony was chosen. For protein expression, yeast culture was grown in buffered glycerol media medium (BMGY) at 28 °C in a shaking incubator until an OD₆₀₀ of ~ 2–6. The yeast cells were harvested through centrifugation and then resuspended in buffered methanol-complex medium (BMMY) containing 1% methanol, followed by growth at 28 °C for 4 days. After the 4-day induction period with methanol, the culture supernatants were collected and purified by Ni-NTA affinity chromatography using a purification buffer consisting of 50 mM Tris, 150 mM NaCl, and 10% glycerol pH 8.0. Fractions collected at different imidazole concentrations were analyzed using 12% SDS-PAGE to confirm the purity of purified RBD proteins (Supplementary Fig 1B). Fractions containing the pure RBD protein were pooled together and subsequently dialyzed against 1X PBS at pH 7.4 overnight at 4 °C. Subsequently, the protein was concentrated using Amicon centrifugal filters (Millipore, Burlington, MA, USA) with a molecular weight cut off of 10 kDa.

Binding affinity assessment using ITC:

The thermodynamic parameters and binding affinity of RBD with the nanobodies were determined through ITC with a Micro Cal ITC200 microcalorimeter (Malvern, Northampton, MA) at 25 °C. Purified RBD and native/mutant nanobody were dialyzed in 1 X PBS at pH 7.4 and 10% glycerol. The nanobody (syringe) at a concentration of 50 µM was titrated against 2.5 µM RBD (cell)⁴⁴. The experimental setup consists of an initial injection of 0.5 µL followed by 13 injections of 2.9 µL of the purified nanobody, into the cell containing RBD protein. The

acquired data were fitted into the single-site binding model to generate the binding isotherm and calculate the dissociation constant (K_D) for the binding. Data processing was carried out using MicroCal analysis software, Malvern, in conjunction with the commercially available Origin 7.0 program.

Production of SARS-CoV-2 pseudovirus:

Human embryonic kidney (HEK-293T) cells (NCCS, India) were used for the transient expression of SARS-CoV-2 spike pseudotyped virus. HEK-293T cells expressing Human angiotensin-converting enzyme-2 (hACE2) and TMPRSS2 were obtained from BEI Resources (NR-55293) and used for the neutralization assays. All cell lines were maintained at 37 °C and 5% CO₂ in high glucose Dulbecco's-modified essential media (DMEM; HiMedia, India) supplemented with 10% fetal bovine serum (FBS; Gibco, USA) and 100 U/mL penicillin and 100 mg/mL streptomycin (HiMedia, India).

The plasmid constructs for the production of pseudotyped lentiviral particles expressing S-protein of SARS-CoV-2 were obtained from the BEI Resources SARS-Related Coronavirus 2, Wuhan-Hu-1 Spike-Pseudotyped Lentiviral Kit V2 (NR- 53816). Pseudovirus particles were produced following the protocol described by ⁶⁴. Briefly, 3×10^6 HEK-293T cells were seeded in 6 well plates prior to the day of transfection. At 70-80% confluency, cells were transiently transfected with different concentrations of the plasmids (NR-53742, NR-52516, NR-52517, NR-52518, and NR-52519) required to produce lentiviral particles using Lipofectamine 2000 (Invitrogen) as per the manufacturer's instructions. After 60 h post-transfection, the culture supernatant containing pseudovirus particles was harvested and filtered using a 0.45 µm filter and stored at -80 °C in smaller aliquots. Furthermore, the virus titer was determined by luciferase assay as mentioned by Crawford et al 2020 ⁶⁴.

Pseudovirus neutralization assay:

To perform the neutralization assay, 96 well plates were coated with 0.1 % gelatine (Himedia TCL-059). HEK-293T cells expressing human ACE2-TMPRSS2 (NR:55293) were seeded at a density of 4×10^4 cells /well. On the following day, a 50 μ M concentration of nanobodies were two-fold serially diluted in 2% DMEM. Serially diluted nanobodies were mixed with an equal volume of diluted virus (8×10^5 RLU/mL) supplemented with 10 mg/mL hexadimethrine bromide (Himedia) and incubated for 1 h at 37 °C in a 5% CO₂ incubator⁶⁵. Subsequently, 200 μ L of each dilution was added to HEK-293T cells expressing human ACE2-TMPRSS2. Then, the plate was incubated at 37 °C in a 5% CO₂ incubator for 60 h. Later, the cell lysate was prepared and used for luciferase assay, as mentioned in Crawford et al 2020⁶⁴. From the clarified cell lysate, 20 μ L of supernatant was mixed with 50 μ L of luciferin substrate (SRL, India) and was added into wells of 96 well white opaque plate (Costar) to estimate the relative luminescence, using Synergy HTX multimode plate reader (Agilent BioTek). The experiment was performed thrice and data points represent the average of a triplicate set of readings. Graphs were prepared using Graph Pad Prism 8.0 software^{64,66}.

Results:

Rationale for *in silico* mutagenesis and generation of an *in house* mutant library:

CDRs of native nanobody interact with RBD and hinder the ACE2 binding and viral entry inside the cell. The native nanobody (H11-H4), originally derived from the H11 parent nanobody, was reported to be raised against RBD in Lamma⁴³. To enhance the binding affinity of native nanobody towards RBD, *in silico* affinity maturation approach was employed for which the amino acids were selected based on structural analysis of native nanobody and RBD complex generated through HADDOCK 2.4. Structural analysis of the complex revealed a major contribution of CDR2 and CDR3 loops in interactions with the RBD (Fig 1B). Furthermore, analysis using PyMol and LigPlot+ disclosed that only Arg52 and Ser57 from

297 CDR2 were contributing in hydrogen bonding (H-bond) with the Glu484 of RBD. Whereas,
 298 CDR3 of the nanobody displayed a robust hydrogen bonding network. The residues His100,
 299 Tyr101, Val102, Tyr104, Leu106, and Asp115 of native nanobody forms H-bond with the
 300 Lys444, Asn448, Tyr449, Asn450, Glu484, Phe490, Gln493, and Ser494 residue of RBD (Fig
 301 1C). Mutagenesis was limited to antigen recognition residues within the limit of 6 Å identified
 302 using PyMol, to minimize impact on molecular stability and enable experimental
 303 characterization with a small number of mutants. The amino acids present in the CDR2 (Arg52,
 304 Ser54, Gly55, Gly56, and, Ser57) and CDR3 (His100, Tyr101, Val102, Ser103, Tyr104,
 305 Leu105, Leu106, and Ser107) were selected and mutated using Coot software to generate an
 306 *in house* library of 112 mutants with single amino acid substitutions in the nanobody (Fig 1D).
 307 The rationale for introducing these mutations was to augment and optimize the contribution of
 308 electrostatic and polar interactions, thereby improving the overall stability and functionality
 309 through a targeted modification in the structure^{17,18}. The energy minimization step was
 310 performed using the CHARMM 27 force field in the Gromacs 2022.2 suite after the
 311 introduction of mutations in the 3D structure of the nanobody. The comparative structural
 312 alignment of the CDR loops of native/mutant nanobodies revealed that mutational changes in
 313 CDR3 not only affected CDR3 but also CDR1 and CDR2. These slight structural changes in
 314 CDRs, presumably affect the binding pattern at the interface of nanobody and RBD,
 315 subsequently increasing and decreasing the binding affinities (Supplementary Fig 3A).

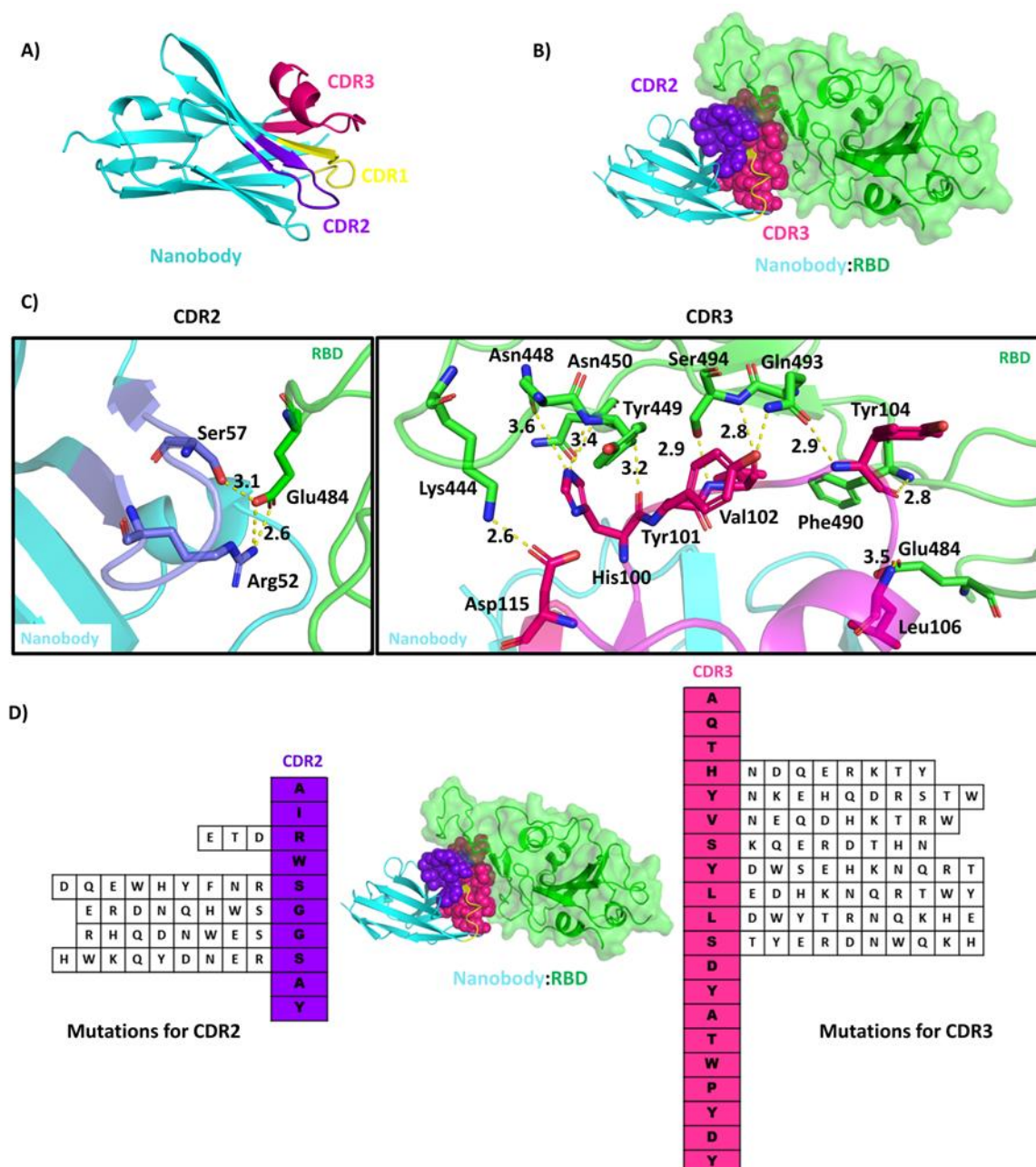


Fig. 1 Detailed structural analysis of nanobody and RBD complex and selection of residue for the *in silico* mutagenesis. A) Cartoon representation of nanobody showing framework region (cyan) and position of CDR1 (yellow), CDR2 (purple), and CDR3 (hot pink). B) Surface representation of RBD (green) and nanobody (cyan) complex generated through HADDOCK 2.4 showing the interacting interface. The CDR2 (purple) and CDR3 (hot pink) regions of nanobody interacting with RBD are depicted as spheres. C) The key interactions present at the interface of RBD (green) and nanobody (cyan) complex generated through HADDOCK 2.4 are

depicted, highlighting the CDR2 (purple) and CDR3 (magenta) of nanobody. Interacting residues of nanobody and RBD are shown in sticks. D) Vertical representation depicts the nanobody residues present in the CDR2 (purple) and CDR3 (hot Pink). The residues selected for *in silico* mutagenesis and library generation from the CDR2 and CDR3 are depicted in horizontal rows (112 mutants).

Selection of the best binders using protein-protein docking and MD simulation:

High-throughput protein-protein docking studies screened and identified the best binders compared to the native nanobody, from an *in house* library of 112 mutants generated against the RBD (Supplementary Table 1) using Coot. Additionally, a comparative analysis of interactions between native/mutated nanobody and RBD docked complexes revealed the formation of new interactions owing to the introduction of certain mutations (Fig 2 and Supplementary Fig 2). Based on interaction examination, out of the 112 mutants studied, 51 showed docking scores comparable to or higher than the native nanobody and formed additional interactions with the RBD, 9 mutants, which had not been previously published were chosen for further characterization. The mutants R52D, S54E, G56H, and S57D were selected for engineering the CDR2 loop, and L105E, L106T, L106Q, S107Q, and S107R were selected from CDR3 for further studies (Table 1). Interestingly, mutation R52D in native nanobody led to the disruption of the salt bridge between Arg52 and Glu484, rather a new H-bond was formed between Asp52 and Gln493 of RBD. For the Ser54 mutations to Glu54, the mutated residue was interacting with the RBD through weak Vander Waal interactions only. The mutation of Gly56 to His56 has imparted changes in the CDR2 loop and pulled Gly55 towards the Gly482 of RBD as observed in PyMol analysis. In native nanobody, Ser57 forms a H-bond with Glu484

of RBD and after mutation of Ser57 to Asp57, this H-bond remained intact. For the CDR3, the mutation of Leu105 to Glu105 resulted in the formation of additional polar interactions with RBD compared to native nanobody. Mutations of Leu106 to Thr106 and Gln106 resulted in polar contacts with the Glu484, the same as of native nanobody and RBD complex. The mutations of Ser107 residue to Arg107 and Gln107 resulted in an additional H-bond with Arg107 and Gly485 of RBD compared to the native nanobody and RBD complex (Fig 2 and Supplementary Fig 2).

Further, for the comparative assessment of the stability and interaction pattern of these selected complexes at the atomistic level, the complexes were subjected to MD simulation studies using a CHARMM 27⁶⁷ force field in the Gromacs 2022.2 suite. The average RMSD of the C α backbone of complexes showed no major fluctuations, the overall values were observed to be below 0.5 Å for all complexes. Low RMSD values suggest the preservation of structural integrity and stability of complexes despite mutational changes in nanobody (Supplementary Fig 3B). The average number of H-bonds formed between RBD and native/mutant nanobody were ~ 6-7 throughout the MD run. For some mutants, the number of H-bonds reached up to ~ 9-10 indicating the formation of new interactions owing to the nature of mutations (Supplementary Fig 3B and Table 1). MD simulation studies indicate rearrangement of the nanobody-RBD interface residues as a result of amino acid changes present in nanobody CDRs (Supplementary Fig 4).

Table 1 Mutations selected for the CDR2 and CDR3 with their docking scores and number of H-bonds based on DimPlot analysis of docked complexes generated through HADDOCK 2.4 and average number of H-bonds calculated after 100 ns MD simulations run.

Mutation	HADDOCK score	No. of H-bond after Docking	No. of average H-bond after MD
Native nanobody	-113.1+/-4.6	9	6.26
R52D	-102.3+/-6.5	5	4.81
S54E	-121.5+/-3.9	14	7.98
G56H	-114.9+/-3.0	9	8.37
S57D	-108.6+/-1.7	10	6.71
L105E	-120.0+/-1.6	13	7.84
L106T	-111.7+/-1.0	11	7.07
L106Q	-111.8+/-2.2	13	7.60
S107Q	-119.0+/-3.1	10	6.98
S107R	-120.0+/-3.0	10	7.45

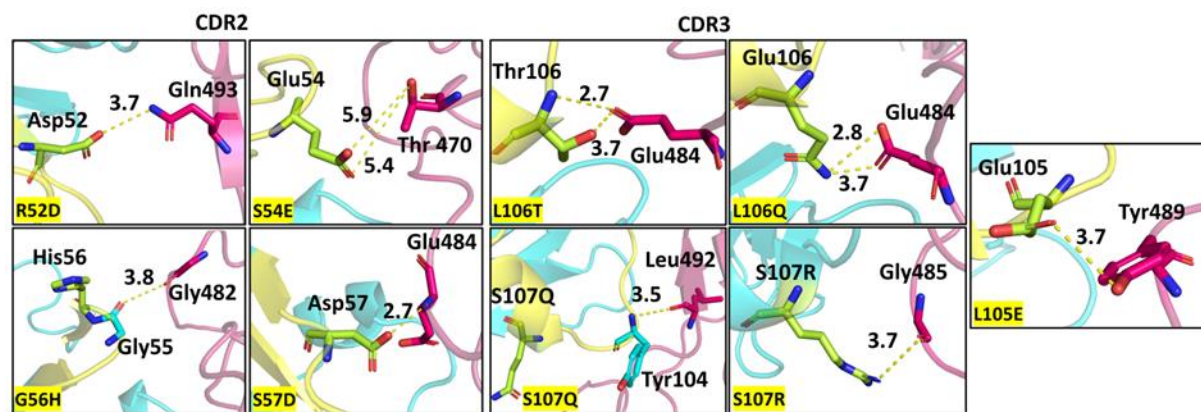
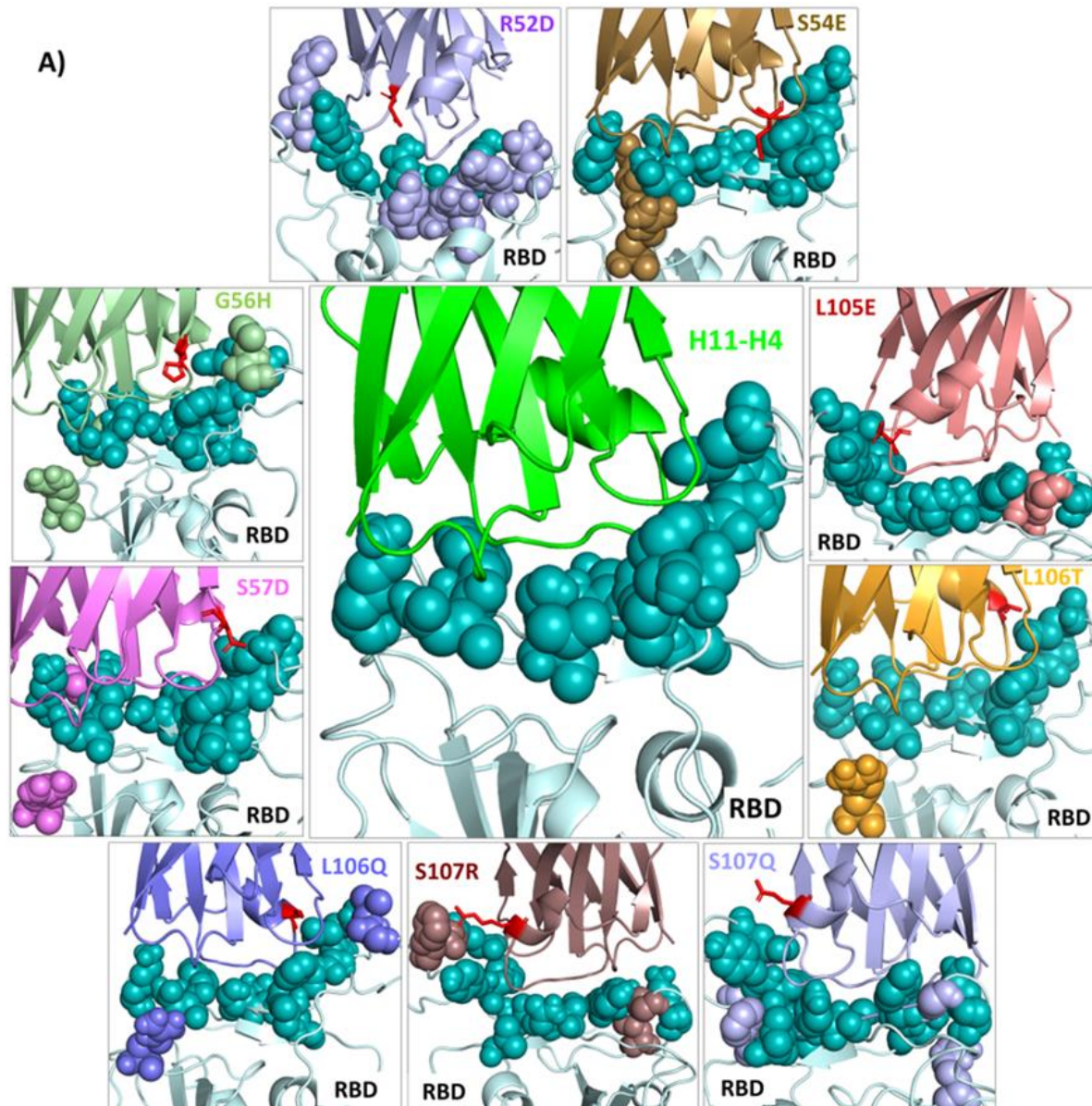


Fig. 2 Protein-protein docking studies reveal differences in interactions of native and mutant nanobodies and RBD complexes. A comprehensive analysis was conducted on mutants of CDR2 and CDR3 of the nanobody in complex with the RBD of SARS-CoV-2, generated using HADDOCK 2.4. The cartoon representation depicts the key interacting residues of a nanobody (cyan) and RBD (light magenta) that were critically studied to understand the effects of the mutations (limon) on the binding affinity. Residues were shown as sticks using PyMol.

Docked complexes of native/mutant nanobody-RBD were analyzed to see the distribution of RBD residue at the interface of the complex within a 4 Å cutoff. All mutants were interacting with the almost same residue stretch on the RBD as the native nanobody. Here, the mutants R52D, G56H, S107Q, and S107R were among the mutants that were targeting some additional residue of RBD as shown in Fig 3. RBD and ACE2 interaction is critical for the life cycle of SARS-CoV-2. Mutations in nanobody disrupting the interaction at the ACE2-RBD interface could operate as promising entry inhibitors for SARS-CoV-2. Interestingly, analysis of RBD and native/mutant nanobody complex revealed that the RBD residues targeted by nanobody were also involved in interaction with ACE2 (Fig 3 and Supplementary Table 3). Additionally,

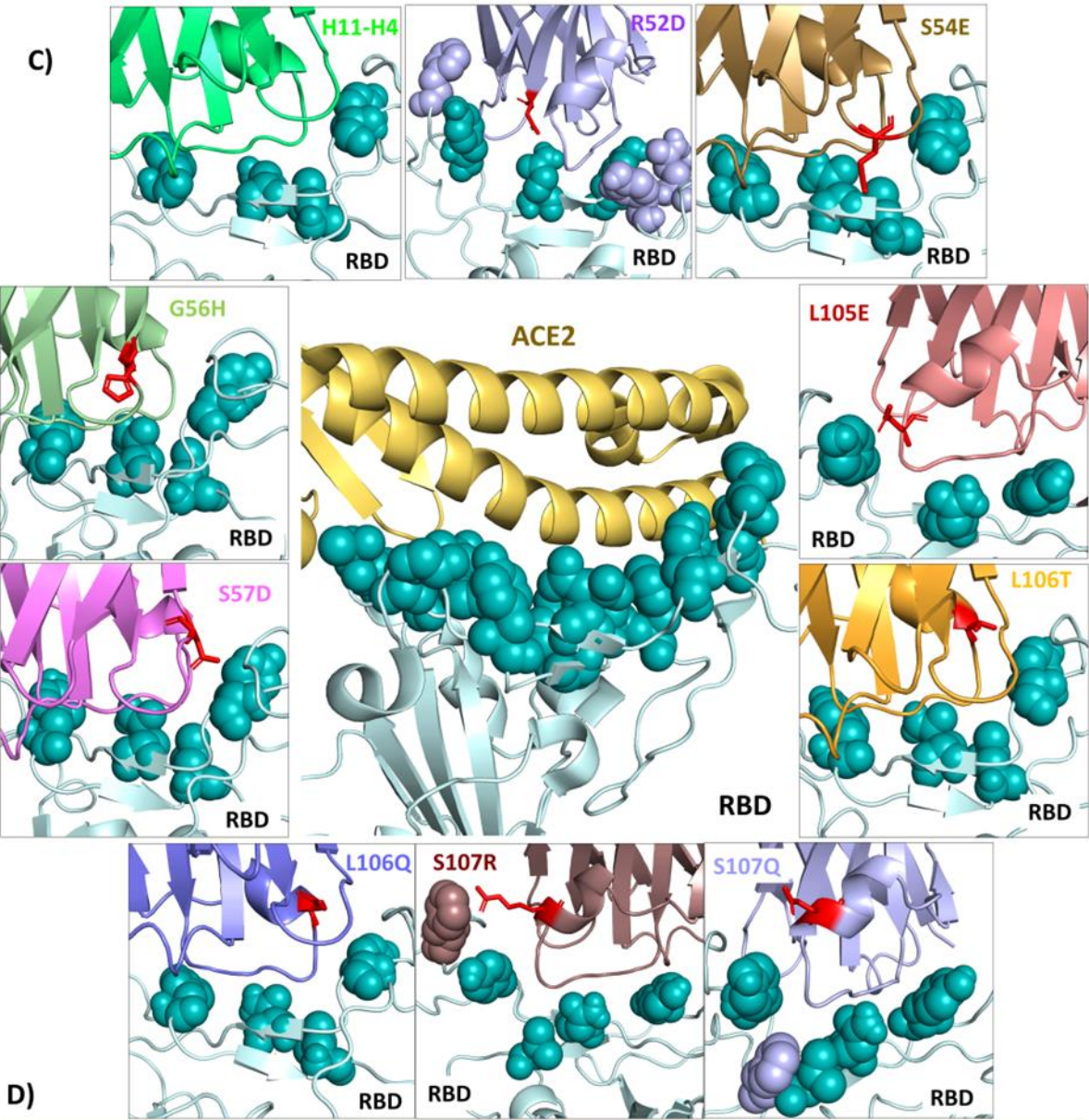
396 a few mutations in nanobody were identified to target some additional residue of the ACE2
397 binding pocket of RBD (Fig 3 and Supplementary Table 3). These mutant nanobodies
398 presumably act like molecular roadblocks, preventing virus entry and infection.

399



B)

RBD residues around 4 Å	
H11-H4	K444, Y449, N450, L452, L455, T470, E484, Y489, F490, L492, Q493, S494
R52D	R403, G446, Y449, Y453, E484, G485, F486, C488, Y489, F490, Q493, S494, Y495, G496, Q498, Y505
S54E	R346, K444, G447, N448, Y449, N450, L455, T470, E484, Y489, F490, Q493, S494
G56H	R346, K444, N448, Y449, N450, L455, G482, V483, E484, Y489, F490, L492, Q493, S494
S57D	R346, K444, G447, Y449, N450, L455, T470, V483, E484, Y489, F490, L492, Q493, S494
L105E	K444, G447, N448, Y449, N450, T470, E484, Y489, F490, L492, Q493, S494
L106T	R346, K444, Y449, N450, L455, E484, Y489, F490, L492, Q493, S494
L106Q	R346, K444, Y449, N450, L455, G482, V483, E484, Y489, F490, L492, Q493, S494
S107Q	R346, K444, G447, Y449, N450, L455, F456, T470, I472, E484, Y489, Q493, S494
S107R	R346, K444, G447, Y449, N450, L455, E484, G485, F486, Y489, F490, L492, Q493, S494



RBD residues around 4 Å	
ACE2	K417, G446, Y449, Y453, L455, F456, A475, F486, N487, Y489, Q493, G496, Q498, T500, N501, G502, Y505
H11-H4	K444, Y449, N450, L452, L455, T470, E484, Y489, F490, L492, Q493, S494
R52D	R403, G446, Y449, Y453, E484, G485, F486, C488, Y489, F490, Q493, S494, Y495, G496, Q498, Y505
S54E	R346, K444, G447, N448, Y449, N450, L455, T470, E484, Y489, F490, Q493, S494
G56H	R346, K444, N448, Y449, N450, L455, G482, V483, E484, Y489, F490, L492, Q493, S494
S57D	R346, K444, G447, Y449, N450, L455, T470, V483, E484, Y489, F490, L492, Q493, S494
L105E	K444, G447, N448, Y449, N450, T470, E484, Y489, F490, L492, Q493, S494
L106T	R346, K444, Y449, N450, L455, E484, Y489, F490, L492, Q493, S494
L106Q	R346, K444, Y449, N450, L455, G482, V483, E484, Y489, F490, L492, Q493, S494
S107Q	R346, K444, G447, Y449, N450, L455, F456, T470, I472, E484, Y489, Q493, S494
S107R	R346, K444, G447, Y449, N450, L455, E484, G485, F486, Y489, F490, L492, Q493, S494

Fig. 3 The comparative analysis of interacting residues at the interface of native and mutant nanobody-RBD complex and ACE2-RBD (PDB: 6MOJ) complex. A) In the native/mutant nanobody-RBD (pale cyan) docked complexes, RBD residues within 4 Å cutoff were shown in teal spheres. For the mutants of nanobody, RBD residues were colour coded in two formats: teal if residues same as native nanobody and in mutation-specific colors. Mutated residue in nanobody were shown in red sticks. B) Tabular representation for RBD residues in a colour coded manner. For the native/mutant nanobody-RBD complex, residues targeted by native nanobody were highlighted in cyan, additional RBD residues targeted by mutants were colour coded as per mutation. C) In the RBD (pale cyan)-ACE2 (yellow orange) complex, RBD residues within the 4 Å cutoff were shown in teal sphere. In the docked complexes of native/mutant nanobody-RBD residues same as of ACE2-RBD complex were shown in teal spheres, while other additional RBD residue were shown in mutation-specific colors. Mutated residue in nanobody were shown in red sticks. D) Tabular representation of the RBD residues within the 4 Å cutoff of ACE2-RBD complex and native/mutant nanobody-RBD complex, highlighting overlapping residues in cyan. Figure prepared using PyMol.

Validation of computational predictions by assessment of binding affinities through ITC:

To establish the accuracy of the *in silico* findings, binding affinities of the mutants with the SARS-CoV-2 RBD were estimated using ITC. The binding titrations of the RBD with the nanobody are exothermically driven. Thermodynamic data generated from ITC isotherms was fitted into a single-site binding model to compare the binding affinities of the native and mutants. Thermodynamic parameters and titration curve depicted that the introduction of mutations such as S54E, S57D, L105E, L106T, L106Q, S107R, and S107Q contributed to the

improved affinities towards the RBD, compared to the native nanobody (Fig 4). Notably, substitutions involving charged or polar residues tend to be particularly effective in improving binding affinity, highlighting the significance of these interactions in computational affinity enhancement, which is consistent with *in silico* findings.

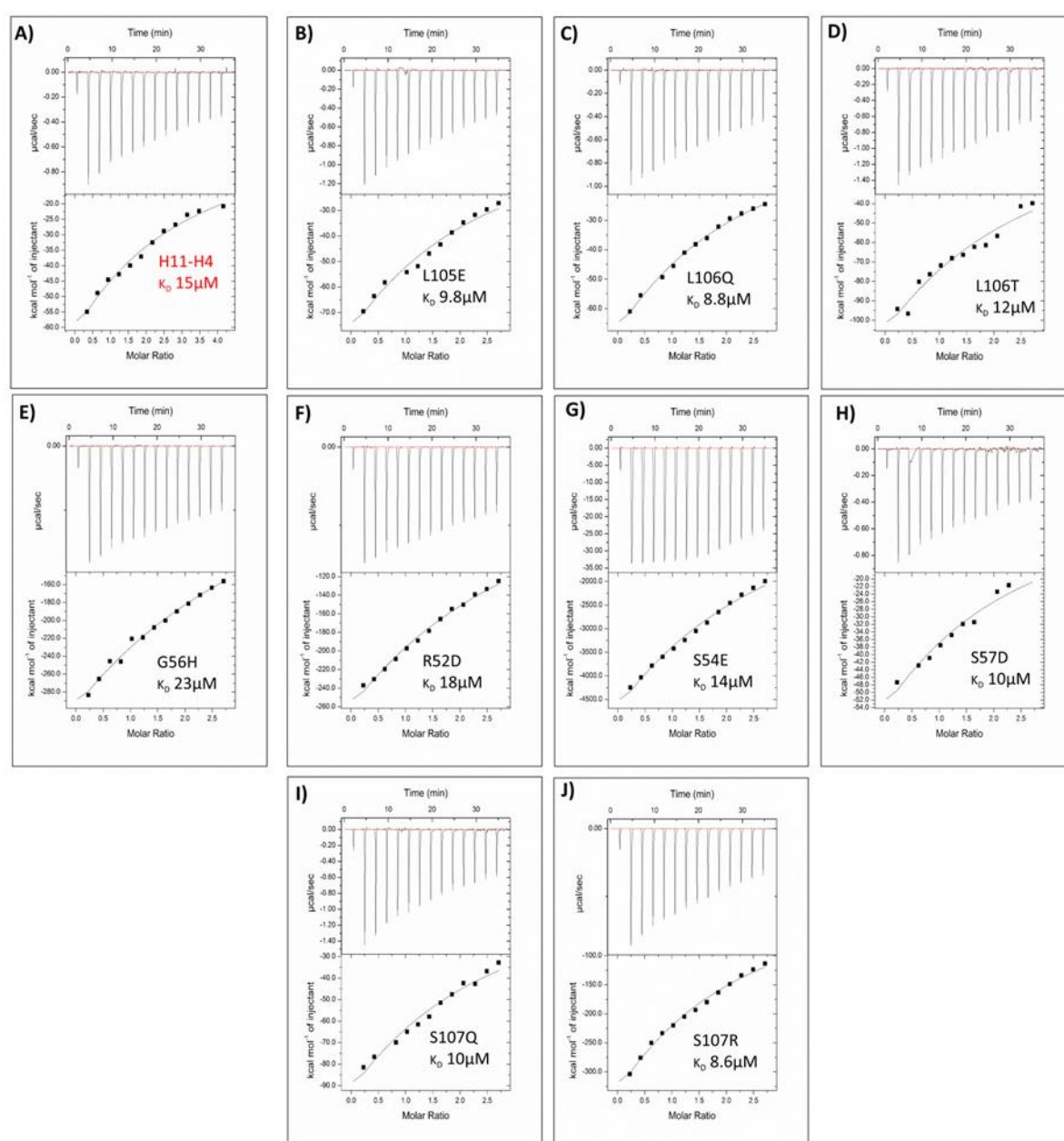


Fig. 4 Determination of binding affinity of native /mutant nanobody with RBD using ITC.

(A-J) Binding isotherm plots were generated using a single-site binding model with the binding affinities of the native/mutants. The upper portion of each ITC titration depicts raw data, while the lower portion displays the fitted binding isotherm, with inset K_D values provided for the native/mutants.

Potent pseudovirus neutralization by generated mutant nanobodies:

The replication of pseudotyped lentiviral particles expressing S-protein successfully mimics SARS-CoV-2 host cell entry ⁶⁴. Consequently, pseudotyped lentiviral particles expressing surface exposed S-protein of SARS-CoV-2 were produced and used to determine the neutralization efficacy of native and the mutant nanobody using HEK-293T cells expressing human ACE2-TMPRSS2. Pseudotyped lentiviral particles were pretreated with increased concentrations of nanobody, and incubated with HEK-293T cells expressing human ACE2-TMPRSS2 for 60 h. The cell lysate was prepared following the method described previously ⁶⁴. The supernatant (20 μ L) from clarified cell lysate was mixed with luciferin substrate (50 μ L/well) in a white opaque 96-well plate. Relative luminescence was measured using a Synergy HTX multimode plate reader (Agilent BioTek). The IC₅₀ values were computed using Graph Pad Prism 8.0 software. The experiment was conducted three times, and each data point represents the average of three readings. Neutralizing efficiency varied considerably among the different mutants with IC₅₀ values ranging from 0.03 -15.27 μ M. Interestingly the mutants L106T, L106Q, S107R, and S107Q have neutralization efficiency significantly better than the native nanobody which is in concordance with the biophysical studies (Fig 5).

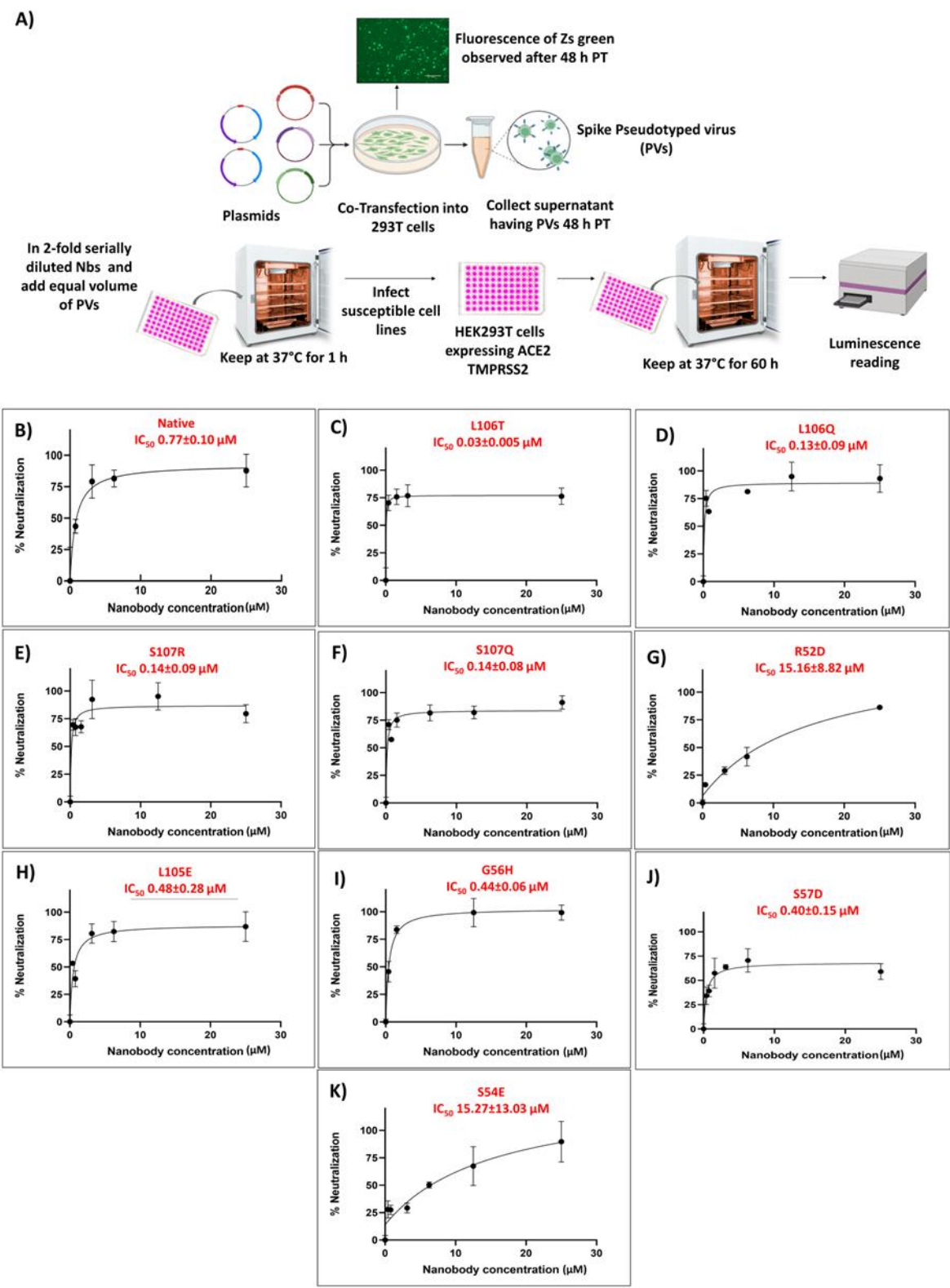


Fig. 5 Evaluation of neutralization efficiency of native and mutant nanobody using pseudovirus assay in HEK-293T cells expressing human ACE2-TMPRSS2. A) Schematic

for the production of SARS-CoV-2 pseudovirus and neutralization assay. (B-K) The neutralization potency of nanobodies were determined using a luciferase based pseudotyped SARS-CoV-2 neutralization assay. Pseudotyped lentiviral particles expressing S-protein of SARS-CoV-2 were pretreated with increased concentrations of nanobody and subsequently incubated with HEK-293T cells expressing human ACE2-TMPRSS2 for 60 h. Post infection, luciferase activity in cell lysates was quantified to calculate IC₅₀ values. The IC₅₀ values were computed using Graph Pad Prism 8.0 software. The experiment was conducted three times, and each data point represents the average of three readings.

Discussion:

The COVID-19 pandemic has impacted the world's population by disrupting social, mental, and economic harmony. The year-long vaccination drive against SARS-CoV-2 has yielded positive results, but the efficacy of current SARS-CoV-2 vaccines and treatments is increasingly challenged by the virus's capacity to evolve. To keep pace with viral evolution, a fast, potent, and cost-effective preventative or therapeutic strategy is the need of the hour. While vaccines prime our immune system to create antibodies against the virus, antibodies-based therapies offer a different approach. They can be directly administered to patients, providing immediate protection or treatment, particularly for those with weakened immune systems who may not respond well to vaccines ⁵.

The success of Caplacizumab, the first FDA-approved nanobody for acquired thrombotic thrombocytopenic purpura (aTTP) treatment, highlights the therapeutic potential of nanobodies. This is further supported by promising results from animal studies using nanobodies as preventative measures (prophylactics) ⁶⁸⁻⁷⁰. Owing to their small molecular

weight, the nanobodies can engage relatively well with large antigenic interfaces. Nanobodies are versatile and easy to manipulate hence serve as good alternatives to conventional antibodies²⁶. In the last two years, several single-domain antibodies i.e. nanobodies have been isolated from the naïve library that binds to the RBD of SARS-CoV-2^{41,43,44}. Nanobodies can be affinity matured for improved binding to target antigens using both experimental and computational tools. *In silico* affinity maturation is robust, efficient, and less laborious compared to conventional methods such as phage display, yeast display, error-prone PCR (Polymerase Chain Reaction), and DNA Shuffling^{22,71}. Mutating the residues of paratopes (antigen-binding site) at the interface of the antigen-antibody complex can significantly impact the complex's affinity. *In silico* affinity maturation strategies often involve structure-guided mutations and the calculation of changes in thermodynamic parameters resulting from these mutations^{21,43,72}. This approach of *in silico* affinity maturation has been successfully applied to antibodies and antibody fragments such as Fab, scFvs, and nanobodies^{17,21,22,71,73,74}.

For an antigen antibody complex, around eighty percent of binding energy is reported to be contributed by a small number of significant interactions, which are predominantly found in the CDRs¹⁷. In earlier reports, methods based on computational prediction such as the ADAPT (Assisted Design of Antibody and Protein Therapeutics) platform, identified 20 to 30 targeted mutations per system to achieve the desired affinity enhancements⁷³. In this study, structure-guided *in silico* mutagenesis pipeline was used for the affinity maturation of the native nanobody, which binds to the RBD of SARS-CoV-2 and hinders the interaction of RBD with ACE2. Detailed structural analysis of the native nanobody and RBD complex revealed the hotspot residue within CDR2 and CDR3, that were further selected for *in silico* mutagenesis and docking studies (Fig 1B). A structure-assisted virtual library of 112 mutants was generated and screened against RBD (Supplementary Table 1). Of the 112 mutants, 9 single mutations were shortlisted, based on docking score, favourable interactions, and MD simulations studies

(Table 1). To validate the findings of *in silico* work, the native /mutates were produced recombinantly used for the *in vitro* evaluation of binding affinities using ITC. In the mutations of CDR2 and CDR3, the formation of additional interactions would have contributed in enhancing the binding affinity towards RBD (Fig 2 and Fig 4). Further, the lentiviral-based pseudovirus neutralization assay identified four potent virus-neutralizing mutants: L106T, L106Q, S107R, and S107Q (0.03 μ M, 0.13 μ M, 0.14 μ M and 0.14 μ M respectively) having improved neutralization potential, compared to the native nanobody ($IC_{50} = 0.77 \mu$ M) (Fig 5).

In previous reports of the native nanobody Arg52 is reported to form a bivalent salt linkage with Glu484. Additionally, this Arg52 is also documented to form a H-bond with the main-chain Ser103 and Tyr109⁴³. Substituting Arg52 with Glu52 disrupted the salt linkage and eventually diminished the binding affinity towards RBD, as reported⁷⁵. Owing to the imperative role of Arg52 in nanobody-RBD interaction, the residue was selected and further subjected to the developed *in silico* pipeline. Intriguingly, mutating Arg52 to Asp52 in the present study resulted in disruption of the salt-bridge as indicated *in silico* studies. In concordance with the *in silico* findings, a decreased binding affinity and neutralization potency was observed for the R52D mutant in comparison to the native nanobody, thereby validating the applicability of the developed pipeline (Fig 5). Across *in silico* and *in vitro* investigations, the mutations most frequently observed in this study entail introducing charged or polar residues into the sequence, which emphasizes the role of these residues in affinity enhancement as also reported earlier^{21,22,76,77}.

Published reports describe the development of optimized antibodies with multiple mutations, ranging from three to fourteen, in their primary sequences, without utilizing electrostatic optimization^{71,78}. In contrast, our approach achieved a 1.5-fold increase in affinity for native nanobody with just a single mutation, which is less likely to alter the 3D structure of nanobody.

In summary, four potential mutants of native H11-H4 nanobody with enhanced affinity against SARS-CoV-2 RBD have been generated in this study using structure- guided *in silico* approach, which is cost effective and less time consuming. Mutations in non-active site residues can significantly impact distant sites, altering substrate specificity through cooperative effects this is well-documented and frequently observed in directed evolution experiments⁷⁹. Mutations in CDR2 and CDR3 might have induced structural changes in CDR1 or the framework region of the nanobody, affecting its affinity and neutralization efficacy upon mutation. Follow up *in vitro* virus-based , *in vivo* mouse model studies and determination of the atomic structure of Ag-Ab complex (RBD and mutant) is next step for the study and will help to unravel the underlying physicochemical inhibitory mechanisms of engineered nanobodies in detail. The developed pipeline can be used easily and effectively to generate CDRs tailored to emerging variants of SARS-CoV-2 in the near future.

Conclusion:

The present study illustrates the potential of computational techniques in refining antibodies for enhanced affinity towards specific antigens, as evidenced by the *in silico* affinity maturation of a native nanobody targeting the RBD of SARS-CoV-2. Identified key mutations that significantly improved the binding affinity showcased the effectiveness of the designed structure-guided *in silico* mutagenesis pipeline. The findings underscore the importance of computational methods in antibody optimization, complemented by rigorous biophysical characterization and *in vitro* efficacy validation. This integrated approach holds promise for accelerating the development of therapeutic interventions against evolving pathogens like SARS-CoV-2 and others.

Acknowledgment

ST and JS acknowledge and thank the Indian Council for Medical Research (ICMR) Government of India (Project. ref no ISRM/12/ (06)/2022) for supporting this study. VS is thankful to ICMR and MB, SC are thankful to the Council of Scientific and Industrial Research (CSIR) for financial support. SKN acknowledges the Ministry of Human Resource Development, (MHRD) for research fellowship. ST, JS and PK thanks the Department of Biotechnology, Govt of India for supporting the Translational and Structural Bioinformatics Centre at Department of Biosciences and Bioengineering, IIT Roorkee (reference number BT/PR40141/BTIS/137/16/2021). Authors also thank Ashok Soota Molecular Medicine Facility and Macromolecular Crystallographic Unit (MCU) at the Indian Institute of Technology Roorkee (IIT Roorkee).

Conflict of Interest

The authors declare that the research was conducted in the absence of any commercial or financial relationships that could be construed as a potential conflict of interest.

Authors contributions:

Conceptualization, S.T., J.S., R.K., and P.K.; methodology, S.T., V.S., M.B., and S.C.; experimentation, V.S., M.B., S.C., and S.K.N.; formal analysis, S.T., J.S., R.K., P.K., VS., M.B., and S.C.; writing- original draft, S.T., V.S., M.B., and S.C., writing-review & editing, S.T., J.S., R.K., and P.K. supervision, S.T., and P.K.; All authors read, revised and approved the manuscript.

References

1. Beck, A. Biosimilar, biobetter and next generation therapeutic antibodies. *MAbs* **3**, 107–110 (2011).
2. Liu, P. *et al.* An Omalizumab Biobetter Antibody With Improved Stability and Efficacy for the Treatment of Allergic Diseases. *Front Immunol* **11**, 596908 (2020).
3. Afzal, A. *et al.* Rapid antibody diagnostics for SARS-CoV-2 adaptive immune response. *Analytical Methods* **13**, 4019–4037 (2021).

- 588 4. Zahavi, D. & Weiner, L. Monoclonal Antibodies in Cancer Therapy. *Antibodies* **9**, 1–
589 20 (2020).
- 590 5. Lai, S. K., Mcsweeney, M. D. & Pickles, R. J. Learning from past failures: Challenges
591 with monoclonal antibody therapies for COVID-19. *Journal of Controlled Release*
592 **329**, (2021).
- 593 6. Pande, J., Szewczyk, M. M. & Grover, A. K. Phage display: concept, innovations,
594 applications and future. *Biotechnol Adv* **28**, 849–858 (2010).
- 595 7. Little, M., Kipriyanov, S. M., Le Gall, F. & Moldenhauer, G. Of mice and men:
596 Hybridoma and recombinant antibodies. *Immunol Today* **21**, 364–370 (2000).
- 597 8. Doria-Rose, N. A. & Joyce, M. G. Strategies to guide the antibody affinity maturation
598 process. *Curr Opin Virol* **11**, 137–47 (2015).
- 599 9. Mishra, A. K. & Mariuzza, R. A. Insights into the structural basis of antibody affinity
600 maturation from next-generation sequencing. *Frontiers in Immunology* vol. 9 Preprint
601 at <https://doi.org/10.3389/fimmu.2018.00117> (2018).
- 602 10. Sulea, T. *et al.* Structure-based dual affinity optimization of a SARS-CoV-1/2 cross-
603 reactive single-domain antibody. *PLoS One* **17**, (2022).
- 604 11. Kim, J., Mcfee, M., Fang, Q., Abdin, O. & Kim, P. M. Computational and artificial
605 intelligence-based methods for antibody development. *Trends Pharmacol Sci* **44**,
606 (2023).
- 607 12. Chan, D. T. Y. & Groves, M. A. T. Affinity maturation: highlights in the application of
608 *in vitro* strategies for the directed evolution of antibodies. *Emerg Top Life Sci* **5**, 601–
609 608 (2021).
- 610 13. Cannon, D. A. *et al.* Experimentally guided computational antibody affinity maturation
611 with de novo docking, modelling and rational design. *PLoS Comput Biol* **15**,
612 e1006980- (2019).
- 613 14. Haidar, J. N. *et al.* A universal combinatorial design of antibody framework to graft
614 distinct CDR sequences: A bioinformatics approach. *Proteins: Structure, Function, and*
615 *Bioinformatics* **80**, 896–912 (2012).
- 616 15. Hanf, K. J. M. *et al.* Antibody humanization by redesign of complementarity-
617 determining region residues proximate to the acceptor framework. *Methods* **65**, 68–76
618 (2014).
- 619 16. Al-Lazikani, B., Lesk, A. M. & Chothia, C. Standard conformations for the canonical
620 structures of immunoglobulins11Edited by I. A. Wilson. *J Mol Biol* **273**, 927–948
621 (1997).
- 622 17. Robin, G. *et al.* Restricted Diversity of Antigen Binding Residues of Antibodies
623 Revealed by Computational Alanine Scanning of 227 Antibody-Antigen Complexes.
624 (2014) doi:10.1016/j.jmb.2014.08.013.
- 625 18. Xin, L. *et al.* Identification of Strategic Residues at the Interface of Antigen-Antibody
626 Interactions by In Silico Mutagenesis. *Interdiscip Sci* **10**, 438–448 (2018).

- 627 19. Boder, E. T., Midelfort, K. S. & Wittrup, K. D. Directed evolution of antibody
628 fragments with monovalent femtomolar antigen-binding affinity. *Proc Natl Acad Sci U*
629 *S A* **97**, 10701–10705 (2000).
- 630 20. Chaudhuri, D., Majumder, S., Datta, J. & Giri, K. Designing of nanobodies against
631 Dengue virus Capsid: a computational affinity maturation approach. *J Biomol Struct*
632 *Dyn* (2022) doi:10.1080/07391102.2022.2029773.
- 633 21. Kiyoshi, M. *et al.* Affinity improvement of a therapeutic antibody by structure-based
634 computational design: generation of electrostatic interactions in the transition state
635 stabilizes the antibody-antigen complex. *PLoS One* **9**, (2014).
- 636 22. Lippow, S. M., Wittrup, K. D. & Tidor, B. Computational design of antibody-affinity
637 improvement beyond in vivo maturation. *Nature Biotechnology* 2007 25:10 **25**, 1171–
638 1176 (2007).
- 639 23. Razai, A. *et al.* Molecular Evolution of Antibody Affinity for Sensitive Detection of
640 Botulinum Neurotoxin Type A. *J Mol Biol* **351**, 158–169 (2005).
- 641 24. Zhou, J. O., Zaidi, H. A., Ton, T. & Fera, D. The Effects of Framework Mutations at
642 the Variable Domain Interface on Antibody Affinity Maturation in an HIV-1 Broadly
643 Neutralizing Antibody Lineage. *Front Immunol* **11**, (2020).
- 644 25. Hamers-Casterman, C. *et al.* Naturally occurring antibodies devoid of light chains.
645 *Nature* **363**, 446–448 (1993).
- 646 26. Sormanni, P., Aprile, F. A. & Vendruscolo, M. Third generation antibody discovery
647 methods: in silico rational design. *Chem Soc Rev* **47**, 9137–9157 (2018).
- 648 27. Muyldermans, S. Nanobodies: Natural Single-Domain Antibodies. *Annu Rev Biochem*
649 **82**, 775–797 (2013).
- 650 28. Yang, E. Y. & Shah, K. Nanobodies: Next Generation of Cancer Diagnostics and
651 Therapeutics. *Front Oncol* **10**, 1182 (2020).
- 652 29. Van Bockstaele, F., Holz, J. B. & Revets, H. The development of nanobodies for
653 therapeutic applications. *Curr Opin Investig Drugs* **10**, 1212–1224 (2009).
- 654 30. Pardon, E. *et al.* A general protocol for the generation of Nanobodies for structural
655 biology. *Nat Protoc* **9**, 674–693 (2014).
- 656 31. Bannas, P., Hambach, J. & Koch-Nolte, F. Nanobodies and nanobody-based human
657 heavy chain antibodies as antitumor therapeutics. *Front Immunol* **8**, 1603 (2017).
- 658 32. Tijink, B. M. *et al.* Improved tumor targeting of anti-epidermal growth factor receptor
659 Nanobodies through albumin binding: taking advantage of modular Nanobody
660 technology. *Mol Cancer Ther* **7**, 2288–2297 (2008).
- 661 33. Markov, P. V *et al.* The evolution of SARS-CoV-2. *Nature Reviews Microbiology* | **21**,
662 361–379 (2023).
- 663 34. Lan, J. *et al.* Structure of the SARS-CoV-2 spike receptor-binding domain bound to the
664 ACE2 receptor. *Nature* **581**, 215–220 (2020).

- 665 35. Liu, Y. & Arase, H. Neutralizing and enhancing antibodies against SARS-CoV-2.
666 *Inflamm Regen* **42**, 58 (2022).
- 667 36. Kleine-Weber, H., Pöhlmann, S. & Hoffmann, M. Spike proteins of novel MERS-
668 coronavirus isolates from North-and West-African dromedary camels mediate robust
669 viral entry into human target cells. (2019) doi:10.1016/j.virol.2019.07.016.
- 670 37. Sajna, K. V. & Kamat, S. Antibodies at work in the time of severe acute respiratory
671 syndrome coronavirus 2. *Cytotherapy* **23**, 101–110 (2021).
- 672 38. Custódio, T. F. *et al.* Selection, biophysical and structural analysis of synthetic
673 nanobodies that effectively neutralize SARS-CoV-2. *Nature Communications* 2020
674 *11:1* **11**, 1–11 (2020).
- 675 39. Esparza, T. J., Martin, N. P., Anderson, G. P., Goldman, E. R. & Brody, D. L. High
676 affinity nanobodies block SARS-CoV-2 spike receptor binding domain interaction with
677 human angiotensin converting enzyme. *Sci Rep* **10**, (2020).
- 678 40. Güttler, T. *et al.* Neutralization of SARS-CoV-2 by highly potent, hyperthermostable,
679 and mutation-tolerant nanobodies. *EMBO J* **40**, (2021).
- 680 41. Hanke, L. *et al.* An alpaca nanobody neutralizes SARS-CoV-2 by blocking receptor
681 interaction. *Nat Commun* **11**, (2020).
- 682 42. Hanke, L. *et al.* Multivariate mining of an alpaca immune repertoire identifies potent
683 cross-neutralizing SARS-CoV-2 nanobodies. *Sci Adv* **8**, (2022).
- 684 43. Huo, J. *et al.* Neutralizing nanobodies bind SARS-CoV-2 spike RBD and block
685 interaction with ACE2. *Nat Struct Mol Biol* **27**, 846–854 (2020).
- 686 44. Huo, J. *et al.* A potent SARS-CoV-2 neutralising nanobody shows therapeutic efficacy
687 in the Syrian golden hamster model of COVID-19. *Nat Commun* **12**, (2021).
- 688 45. Koenig, P. A. *et al.* Structure-guided multivalent nanobodies block SARS-CoV-2
689 infection and suppress mutational escape. *Science* **371**, (2021).
- 690 46. Tang, Q., Owens, R. J. & Naismith, J. H. Structural Biology of Nanobodies against the
691 Spike Protein of SARS-CoV-2. *Viruses* **13**, (2021).
- 692 47. Xiang, Y. *et al.* Versatile and multivalent nanobodies efficiently neutralize SARS-CoV-
693 2. *Science* (1979) **370**, 1479–1484 (2020).
- 694 48. Yang, J. *et al.* Computational design and modeling of nanobodies toward SARS-CoV-2
695 receptor binding domain. *Chem Biol Drug Des* **98**, 1–18 (2021).
- 696 49. Wrapp, D. *et al.* Structural Basis for Potent Neutralization of Betacoronaviruses by
697 Single-Domain Camelid Antibodies. *Cell* **181**, 1004-1015.e15 (2020).
- 698 50. Flores-Vega, V. R. *et al.* SARS-CoV-2: Evolution and Emergence of New Viral
699 Variants. *Viruses* 2022, Vol. 14, Page 653 **14**, 653 (2022).
- 700 51. Dubey, A., Choudhary, S., Kumar, P. & Tomar, S. Emerging SARS-CoV-2 Variants:
701 Genetic Variability and Clinical Implications. *Curr Microbiol* **79**, 20 (2021).

- 702 52. Gan, H. H., Twaddle, A., Marchand, B. & Gunsalus, K. C. Structural Modeling of the
703 SARS-CoV-2 Spike/Human ACE2 Complex Interface can Identify High-Affinity
704 Variants Associated with Increased Transmissibility. *J Mol Biol* **433**, 167051 (2021).
- 705 53. Berman, H. M. *et al.* The Protein Data Bank. *Nucleic Acids Res* **28**, 235–242 (2000).
- 706 54. Emsley, P., Lohkamp, B., Scott, W. G. & Cowtan, K. Features and development of
707 Coot. *Acta Crystallogr D Biol Crystallogr* **66**, 486–501 (2010).
- 708 55. PyMOL | pymol.org. Preprint at <https://pymol.org/2/>.
- 709 56. Laskowski, R. A. & Swindells, M. B. LigPlot+: multiple ligand-protein interaction
710 diagrams for drug discovery. *J Chem Inf Model* **51**, 2778–2786 (2011).
- 711 57. Van Zundert, G. C. P. *et al.* The HADDOCK2.2 Web Server: User-Friendly Integrative
712 Modeling of Biomolecular Complexes. *J Mol Biol* **428**, 720–725 (2016).
- 713 58. Van Der Spoel, D. *et al.* GROMACS: fast, flexible, and free. *J Comput Chem* **26**,
714 1701–1718 (2005).
- 715 59. Jaiswal, G. & Kumar, V. In-silico design of a potential inhibitor of SARS-CoV-2 S
716 protein. *PLoS One* **15**, (2020).
- 717 60. Magar, R., Yadav, P. & Barati Farimani, A. Potential neutralizing antibodies discovered
718 for novel corona virus using machine learning. *Sci Rep* **11**, (2021).
- 719 61. Yoon, H. J. *et al.* Exploring sterol transportation behavior of the Niemann-Pick C1-like
720 1 protein with V55L mutation: Sterol-NPC1L1 N-terminal binding energy estimation
721 via molecular dynamics simulations. *International Journal of Modelling and*
722 *Simulation* (2023) doi:10.1080/02286203.2023.2265543.
- 723 62. Vanommeslaeghe, K. *et al.* CHARMM General Force Field: A Force Field for Drug-
724 Like Molecules Compatible with the CHARMM All-Atom Additive Biological Force
725 Fields. *J Comput Chem* **31**, 671–690 (2010).
- 726 63. Arbeitman, C. R. *et al.* Structural and functional comparison of SARS-CoV-2-spike
727 receptor binding domain produced in *Pichia pastoris* and mammalian cells. *Sci Rep* **10**,
728 21779 (2020).
- 729 64. Crawford, K. H. D. *et al.* Protocol and Reagents for Pseudotyping Lentiviral Particles
730 with SARS-CoV-2 Spike Protein for Neutralization Assays. *Viruses* **12**, (2020).
- 731 65. Changela, A. *et al.* Crystal Structure of Human Antibody 2909 Reveals Conserved
732 Features of Quaternary Structure-Specific Antibodies That Potently Neutralize HIV-1.
733 *J Virol* **85**, 2524–2535 (2011).
- 734 66. Garcia-Beltran, W. F. *et al.* COVID-19-neutralizing antibodies predict disease severity
735 and survival. *Cell* **184**, 476-488.e11 (2021).
- 736 67. Lindahl, E., Bjelkmar, P., Larsson, P., Cuendet, M. A. & Hess, B. Implementation of
737 the charmm force field in GROMACS: Analysis of protein stability effects from
738 correction maps, virtual interaction sites, and water models. *J Chem Theory Comput* **6**,
739 459–466 (2010).

68. Detalle, L. *et al.* Generation and Characterization of ALX-0171, a Potent Novel Therapeutic Nanobody for the Treatment of Respiratory Syncytial Virus Infection. *Antimicrob Agents Chemother* **60**, 6–13 (2015).
69. Cardoso, F. M. *et al.* Single-Domain Antibodies Targeting Neuraminidase Protect against an H5N1 Influenza Virus Challenge. *J Virol* **88**, 8278–8296 (2014).
70. Scully, M. *et al.* Caplacizumab Treatment for Acquired Thrombotic Thrombocytopenic Purpura. *N Engl J Med* **380**, 335–346 (2019).
71. Clark, L. A. *et al.* Affinity enhancement of an in vivo matured therapeutic antibody using structure-based computational design. *Protein Sci* **15**, 949 (2006).
72. Cannon, D. A. *et al.* Experimentally guided computational antibody affinity maturation with de novo docking, modelling and rational design. *PLoS Comput Biol* **15**, (2019).
73. Vivcharuk, V. *et al.* Assisted Design of Antibody and Protein Therapeutics (ADAPT). *PLoS One* **12**, (2017).
74. Yoshida, K. *et al.* Exploring designability of electrostatic complementarity at an antigen-antibody interface directed by mutagenesis, biophysical analysis, and molecular dynamics simulations. *Scientific Reports* **2019 9:1** **9**, 1–11 (2019).
75. Mikolajek, H. *et al.* Correlation between the binding affinity and the conformational entropy of nanobody SARS-CoV-2 spike protein complexes. *Proc Natl Acad Sci U S A* **119**, (2022).
76. Marvin, J. S. & Lowman, H. B. Redesigning an antibody fragment for faster association with its antigen. *Biochemistry* **42**, 7077–83 (2003).
77. Selzer, T., Albeck, S. & Schreiber, G. Rational design of faster associating and tighter binding protein complexes. *Nature Structural Biology* **2000 7:7** **7**, 537–541 (2000).
78. Midelfort, K. S. *et al.* Substantial Energetic Improvement with Minimal Structural Perturbation in a High Affinity Mutant Antibody. *J Mol Biol* **343**, 685–701 (2004).
79. Arnold, F. H. Directed Evolution: Bringing New Chemistry to Life. *Angew Chem Int Ed Engl* **57**, 4143–4148 (2018).

Supplementary Tables

Supplementary Table 1: The docking score, number of salt bridge and hydrogen bond contacts calculated using Dimplot for the 112 mutations generated using Coot on CDR2 and CDR3 loops of native nanobody. Mutants selected for further MD simulation studies are highlighted in light green.

	Mutation	HADDOCK score	Number of Hydrogen bonds	Number of Salt bridge
	Native nanobody (Reference)	-113.1+/-4.6	9	0
1.	R52D	-102.3+/-6.5	5	0
2.	R52E	-103.5+/-7.4	6	0
3.	R52S	-101.4+/-1.8	5	2
4.	S54R	-119.7+/-3.7	10	0
5.	S54N	-116.9+/-1.2	11	1
6.	S54D	-118.3+/-2.0	10	0
7.	S54Q	-117.0+/-2.6	9	0
8.	S54E	-121.5+/-3.9	14	0
9.	S54H	-118.1+/-1.6	12	0
10.	S54F	-116.4+/-0.8	8	1
11.	S54Y	-125.3+/-2.8	9	0
12.	S54W	-126.1+/-1.5	11	0
13.	G55R	-113.7+/-5.1	6	0
14.	G55S	-112.9+/-1.0	8	1
15.	G55H	-122.7+/-2.0	10	0
16.	G55E	-98.5+/-7.2	9	0
17.	G55Q	-110.5+/-1.1	11	0
18.	G55D	-113.6+/-1.7	10	0
19.	G55N	-118.1+/-1.6	12	0
20.	G55W	-128.7+/-2.3	10	0
21.	G56N	-112.1+/-2.6	8	0
22.	G56Q	-116.9+/-1.5	11	0
23.	G56R	-113.6+/-1.5	9	0
24.	G56D	-111.0+/-2.3	10	0
25.	G56E	-92.8+/-5.0	3	0
26.	G56H	-114.9+/-3.0	9	0
27.	G56S	-113.2+/-1.7	6	1
28.	G56W	-114.7+/-1.5	9	0
29.	S57R	-108.9+/-7.9	11	0
30.	S57Y	-121.5+/-3.8	8	1
31.	S57W	-114.8+/-3.2	8	0
32.	S57K	-119.4+/-4.3	11	1
33.	S57H	-125.9+/-2.1	10	0
34.	S57E	-95.8+/-1.8	5	0
35.	S57Q	-92.0+/-1.8	4	0
36.	S57D	-108.6+/-1.7	10	0

37.	S57N	-118.3+/-4.7	12	0
38.	H100D	-112.9+/-3.4	8	0
39.	H100E	-117.7+/-2.6	7	1
40.	H100N	-104.1+/-1.5	9	0
41.	H100K	-107+/-1.7	8	0
42.	H100Y	-111.1+/-0.7	10	0
43.	H100T	-109.3+/-0.7	11	0
44.	H100Q	-113.2+/-2.7	9	1
45.	H100R	-111.9+/-0.1	10	0
46.	Y101K	-109.9+/-1.3	8	1
47.	Y101N	-112.2+/-0.3	7	0
48.	Y101S	-110.9+/-3.0	9	1
49.	Y101E	-108.3+/-4.9	10	0
50.	Y101D	-95.3+/-3.5	10	0
51.	Y101W	-100.7+/-2.0	3	0
52.	Y101R	-105.5+/-2.8	11	0
53.	Y101Q	-99.2+/-1.3	7	0
54.	Y101H	-97.5+/-3.9	7	0
55.	Y101T	-120+/-3.5	10	0
56.	V102W	-120.7+/-1.3	7	1
57.	V102R	-108.6+/-5.5	7	0
58.	V102Q	-105.5+/-2.4	8	0
59.	V102K	-109.2+/-2.9	10	1
60.	V102N	-97.6+/-1.1	5	0
61.	V102H	-116.3+/-3.7	10	0
62.	V102E	-96.8+/-2.8	6	0
63.	V102D	-110.7+/-1.1	9	1
64.	V102T	-109.4+/-1.3	7	1
65.	S103E	-122.1+/-3.7	11	1
66.	S103R	-122.1+/-1.8	11	0
67.	S103T	-123.5+/-1.3	12	0
68.	S103D	-117.2+/-3.7	11	0
69.	S103H	-116.5+/-2.5	9	0
70.	S103N	-113.8+/-1.8	10	1
71.	S103Q	-119.3+/-1.0	12	0
72.	S103K	-114.2+/-2.0	5	1
73.	Y104E	-91.7+/-2.0	4	1
74.	Y104H	-96.8+/-4.7	7	0
75.	Y104K	-95.9+/-6.3	4	1
76.	Y104N	-83.4+/-4.0	6	0
77.	Y104S	-106.5+/-0.7	13	0
78.	Y104Q	-91.8+/-6.2	11	1
79.	Y104R	-88.4+/-5.7	6	1
80.	Y104D	-91.3 +/- 3.2	5	2
81.	Y104W	-107.6+/-1.3	5	0
82.	Y104T	-107.0 +/- 2.8	12	0
83.	L105D	-113.7+/-2.3	11	0
84.	L105E	-120.0+/-1.6	13	0

85.	L105R	-113.2+/-2.8	9	0
86.	L105N	-115.8+/-3.7	12	0
87.	L105H	-119.1+/-6.3	11	0
88.	L105Q	-114.5+/-2.3	10	1
89.	L105K	-115.2+/-3.3	10	0
90.	L105T	-115.0+/-1.6	12	1
91.	L105Y	-125.2+/-3.2	10	0
92.	L105W	-133.3+/-1.7	10	1
93.	L106W	-106.6+/-2.7	5	1
94.	L106Y	-94.8+/-4.0	6	0
95.	L106T	-111.7+/-1.0	11	0
96.	L106R	-90.5+/-3.4	3	1
97.	L106Q	-111.8+/-2.2	13	0
98.	L106N	-114.8+/-4.0	11	0
99.	L106K	-114.7 +/- 6.6	11	0
100.	L106H	-111.9+/-6.0	9	1
101.	L106E	-94.6+/-3.8	8	0
102.	L106D	-90.8+/-3.7	5	0
103.	S107E	-117.1+/-1.5	8	1
104.	S107T	-117.3+/-3.0	11	0
105.	S107Y	-125.2+/-3.1	12	0
106.	S107N	-118.2+/-1.8	9	0
107.	S107Q	-119.0+/-3.1	10	0
108.	S107K	-117.5+/-2.0	9	0
109.	S107H	-121.0+/-1.0	10	1
110.	S107R	-120.0+/-3.0	10	0
111.	S107W	-128.6+/-4.6	10	0
112.	S107D	-114.8 +/- 2.1	8	0

781

782

783

784

785

786

787

788

789

790

791

792

793

794 **Supplementary Table 2:** Set of primers used for the Site Directed Mutagenesis of native
795 nanobody.

796

S. no.	Mutations	Forward primer	Reverse Primer
1.	R52D	TTGCAGCAATTGATTGGAGCGG TGGTAGCGCATA	CCACCGCTCCAATCAATTGCT GCAACAAATTCACG
2.	S54E	GCAATTCGTTGGGAAGGTGGTA GCGCATATTATGCAGA	ATAATATGCGCTACCACCTTC CCAACGAATTGCTGCA
3.	G56H	CGTTGGAGCGGTCATAGCGCAT ATTATGCAGATAG	AATATGCGCTATGACCGCTCC AACGAATTGCTGC
4.	S57D	GCAATTCGTTGGAGCGGTGGTG ATGCATATTATG	ACGCTATCTGCATAATATGCAT CACCACCGCTCC
5.	L105E	CGCAGACCCATTATGTTAGCTAT GAACTGAGCGATTATG	GGCCAGGTTGCATAATCGCTC AGTTCATAGCTAACATAA
6.	L106Q	CCCATTATGTTAGCTATCTGCAG AGCGATTATGC	CCAGGTTGCATAATCGCTCTG CAGATAGCTAA
7.	L106T	GCAGACCCATTATGTTAGCTATC TGACCAGCGATTATGC	GGCCAGGTTGCATAATCGCTG GTCAGATAGCTAACAT
8.	S107Q	CCCATTATGTTAGCTATCTGCTG CAGGATTATGCAACCT	CGGCCAGGTTGCATAATCCTG CAGCAGATAGCTAACATA
9.	S107R	CCATTATGTTAGCTATCTGCTGC GTGATTATGCAACCT	GGCCAGGTTGCATAATCACGC AGCAGATAGCTAAC

797

798

799

Supplementary Table 3: The distribution of RBD residues within 4 Å cutoff of native/mutant nanobody-RBD docked complexes and ACE2-RBD (PDB: 6MOJ) complex in colour coded manner. Here boxes adjacent to RBD residue were coloured light blue if they are present in indicated complex otherwise left blank.

804

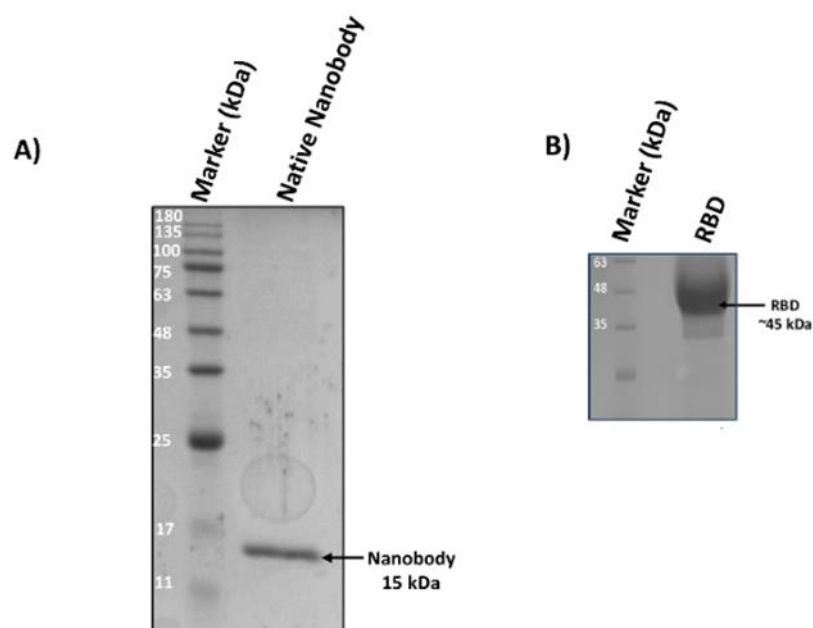
805

RBD Residue	RBD-ACE2	RBD-Native	RBD-R52D	RBD-S54E	RBD-G56H	RBD-S57D	RBD-L105E	RBD-L106T	RBD-L106Q	RBD-S107Q	RBD-S107R
R346											
R403											
K417											
K444											
G446											
G447											
N448											
Y449											
N450											
L452											
Y453											
L455											
F456											
T470											
I472											
A475											
G482											
V483											
E484											
G485											
F486											
N487											
C488											
Y489											
F490											
L492											
Q493											
S494											
Y495											
G496											
Q498											
T500											
N501											
G502											
Y505											

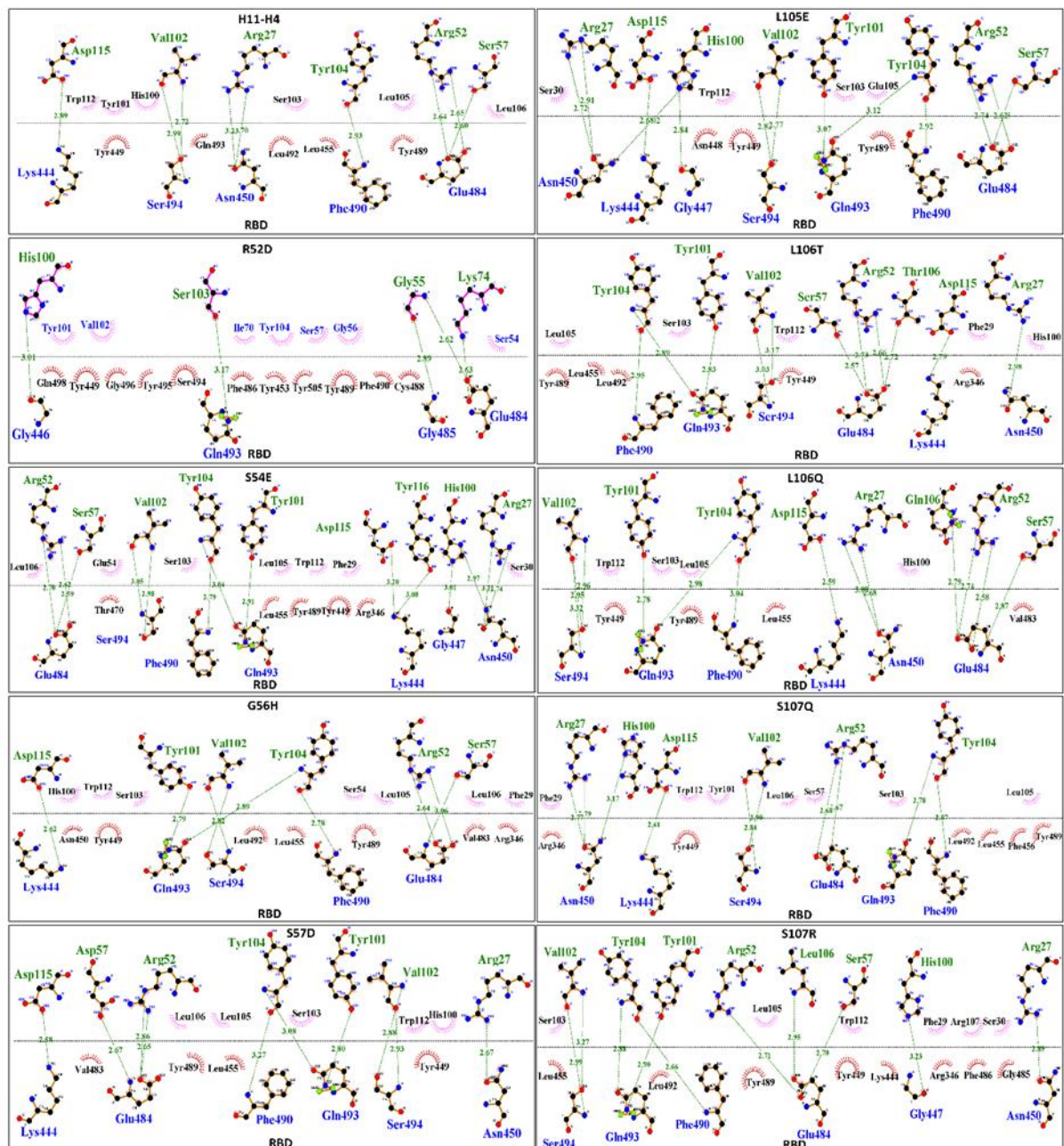
806

807

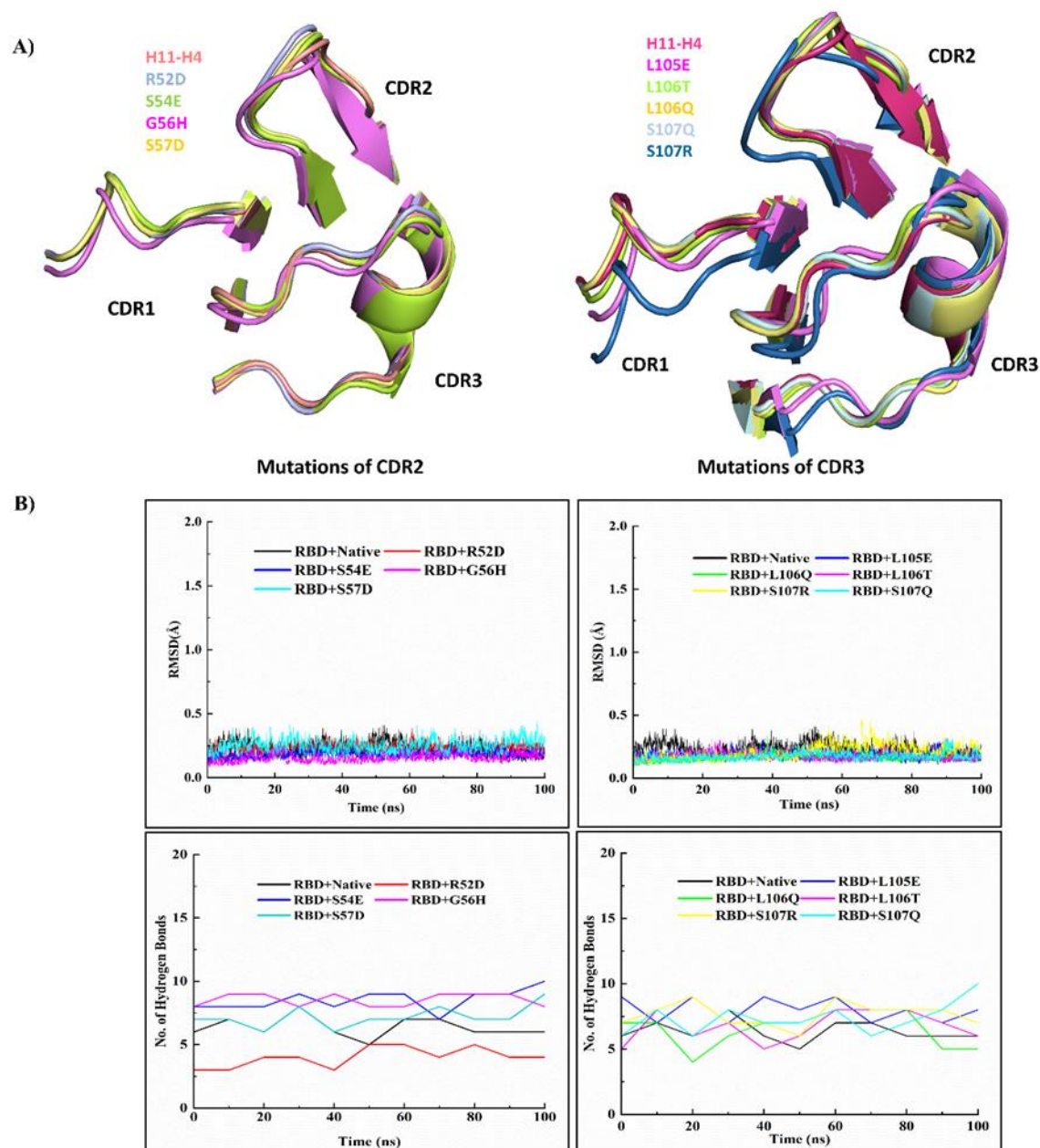
Supplementary Figures



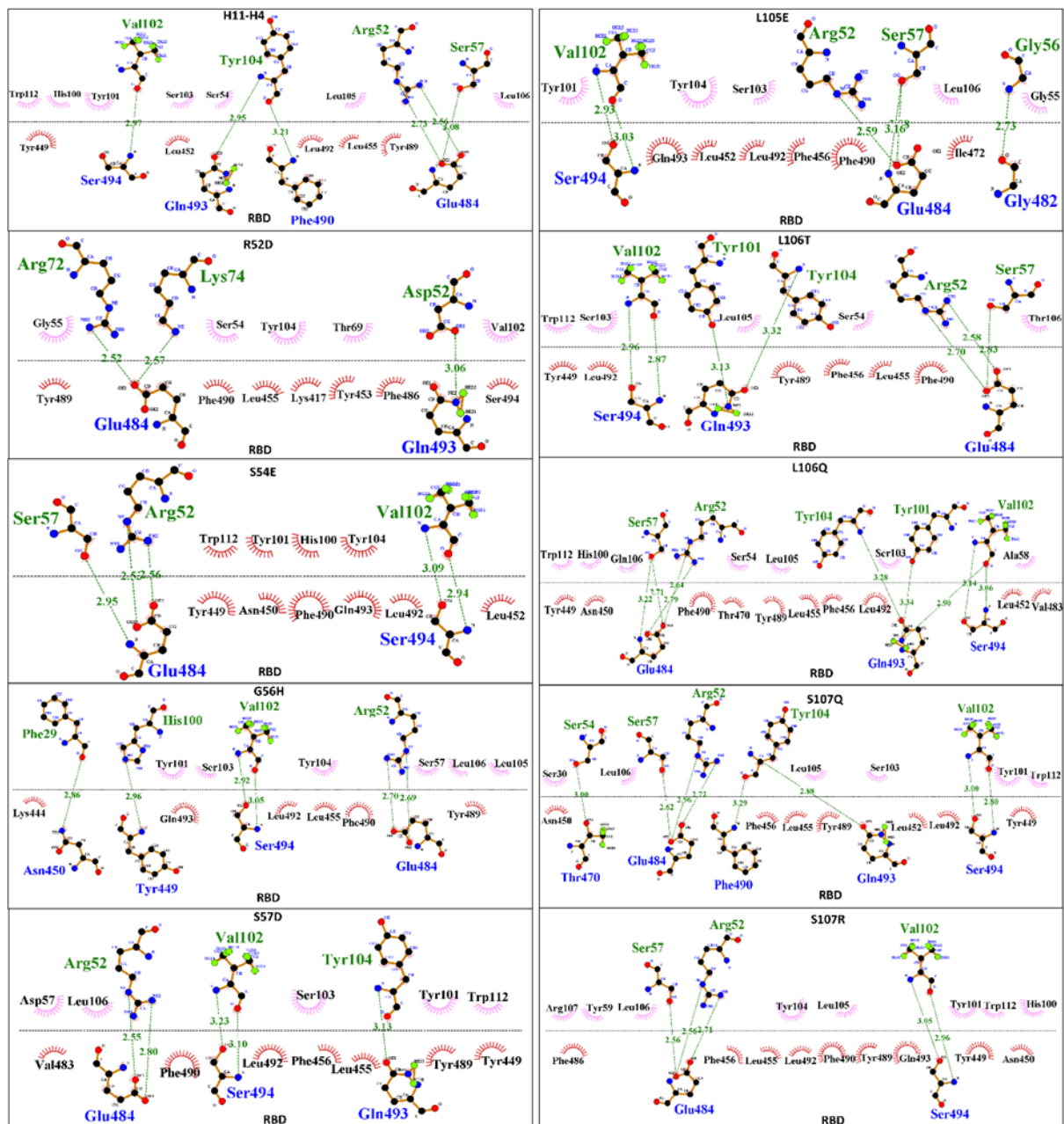
Supplementary Fig 1: SDS-PAGE profile for the purification of native nanobody and RBD proteins. A) Lane 1: marker (180 kDa); Lane 2: native nanobody (15 kDa). B) Lane 1: marker; Lane 2: RBD (~ 45 kDa).



Supplementary Fig 2: 2D schematic representation of nanobody and RBD interacting residues generated through DimPlot. The docked complex of nanobody and RBD generated using HADDOCK 2.4 was used for the preparation of DimPlots. Hydrogen bonds are depicted by green dashed lines connecting the atoms involved, with the donor-acceptor distance indicated in Å. Hydrophobic contacts are shown as red arcs with spokes extending towards the atoms they interact with.



Supplementary Fig 3: Structural superimposition of CDRs and analysis of MD simulations trajectories. A) CDRs of energy minimized structure of native and mutants for CDR2 and CDR3 were superimposed using PyMol. B) For the CDR2 and CDR3 the MD simulations trajectories were used to generate RMSD Plot for the native/mutant nanobody in complex with RBD and number of H-bonds formed between the native/mutant nanobody and RBD throughout 100 ns MD run.



Supplementary Fig 4: 2D schematic representation of nanobody and RBD interacting residues generated through DimPlot. The frame PBDs were extracted from the MD run trajectories and used for the generation of DimPlots. Hydrogen bonds are depicted by green dashed lines connecting the atoms involved, with the donor-acceptor distance indicated in Å. Hydrophobic contacts are shown as red arcs with spokes extending towards the atoms they interact with.

844

845

846

847

848